Exp Fluids (2015) 56:216
DOI 10.1007/s00348-015-2084-6

RESEARCH ARTICLE

Temporally optimized spanwise vorticity sensor measurements in turbulent boundary layers

C. Morrill-Winter[1] · J. Klewicki[1,2] · R. Baidya[1] · I. Marusic[1]

Abstract Multi-element hot-wire anemometry was used to measure spanwise vorticity fluctuations in turbulent boundary layers. Smooth wall boundary layer profiles, with very good spatial and temporal resolution, were acquired over a Kármán number range of 2000–12,700 at the Melbourne Wind Tunnel at the University of Melbourne and the University of New Hampshire's Flow Physics Facility. A custom hot-wire probe was necessary to simultaneously obtain velocity and spanwise vorticity measurements centered at a fixed point in space. A custom calibration/processing scheme was developed to utilize single-wall-parallel wires to optimize the accuracy of the measured wall-normal velocity fluctuations derived from the sensor's ×-array.

1 Introduction

Wall turbulence is comprised of a range of scales, eddies, that are energetically sustained through a sequence of similar characteristic interactions. Within the turbulence, these features are nominally repeated. Ensembles of these recurring interactions over time-scales larger than the integral scales of turbulence underlie the observed behavior of the mean dynamics. For statistically stationary flows, the mean dynamics are most commonly described by an unclosed momentum transport equation; i.e., the mean momentum balance (MMB). The mechanisms that describe the variations in the terms of this equation are of primary concern to turbulence research and modeling. The mechanisms represented in the MMB are strongly influenced by the mean vorticity and velocity-vorticity correlations. This is apparent when the mean boundary layer equation for flat plate flow is written as follows.

$$U\frac{\partial U}{\partial x} - V\Omega_z + \overline{w\omega_y} - \overline{v\omega_z} + \nu\frac{\partial \Omega_z}{\partial y} = 0 \quad (1)$$

Herein u, v and w are the streamwise, wall-normal, and spanwise components of velocity respectively, and ω is vorticity, where the subscript denotes the component direction. Upper and lower case letters signify mean quantities and the fluctuations about that mean, respectively.

In Eq. 1, the Reynolds stress gradient becomes $\bar{l}_x = \overline{w\omega_y} - \overline{v\omega_z}$, which is exact in a channel, and is well approximated in a boundary layer with large overall scale separation. This scale separation is conveniently quantified by the Kármán number, $\delta\nu/u_\tau$, where δ is the boundary layer thickness, the friction velocity $u_\tau = (\tau_w/\rho)^{1/2}$ is the square-root of the wall shear stress on density, and ν is the kinematic viscosity of the fluid. A superscript + denotes normalization by these variables. As originally suggested by Hinze (1975), the x-component of the Lamb-vector, $\bar{l}_x$, is likened to the active vortical component of the totality of motions proposed by Townsend (1976). A primary goal of turbulence research is to devise a way to close Eq. 1. Therefore, in the case of boundary layer research, an understanding of the velocity-vorticity products can give valuable insight into to physical mechanisms associated with the unclosed term. Existing evidence indicates that with increasing δ^+ the scale separation between the velocity and vorticity field increases, and thus the closure problem is directly related to the interaction of these increasingly

✉ C. Morrill-Winter
caleb.morrillwinter@gmail.com

1 Department of Mechanical Engineering, University of Melbourne, Melbourne, VIC, Australia

2 Mechanical Engineering Department, University of New Hampshire, Durham, NH, USA

disparate scales of motion (Priyadarshana et al. 2007; Morrill-Winter and Klewicki 2013; Chin et al. 2014).

The measurement of vorticity fluctuations in boundary layers at high δ^+ is challenging. This is largely due to the need to estimate derivatives at high spatial resolution. There have been many researchers who have tried to measure vorticity. Wallace and Foss (1995) provided a review of such research. Apart from a few atmospheric surface layer measurements (Priyadarshana et al. 2007; Folz and James 2010) most of the published data is at δ^+ less than the DNS study of Sillero et al. (2013). The aim of the present study is to acquire well-resolved vorticity fluctuations in high Reynolds number boundary layers and with spatial and temporal resolution sufficient to resolve the full range of vortical motions. Due to configuration complexity and sensing volume size requirements, the present study focuses on a sensor that solely measures the spanwise vorticity. In the following we describe the sensor and its calibration, as well as the facilities employed. This is followed by a presentation of basic statistics and an assessment of the sensor's capabilities.

2 Methodology

Hot-wire anemometry was chosen for this study because of its ability to achieve high spatial and temporal resolution while maintaining the high signal to noise ratios essential for accurate differencing. Although, only ensemble averaged statistics will be presented herein, the data are part of a larger study specific to the study of spanwise vorticity fluctuations for which hot-wires are the most appropriate option. Scaling arguments and empirical evidence suggest that the characteristic inner-normalized length scale of the spanwise vorticity motions are $\mathcal{O}[(\delta^+)^{1/2}]$ for the entirety of the boundary layer (Morrill-Winter and Klewicki 2013). To accurately measure ω_z at scales much smaller than $\mathcal{O}[(\delta^+)^{1/2}]$ with conventional sensors ($\sim$0.5 mm), large viscous scales are helpful, while the temporal resolution of the sensor also has to be greater than the highest frequencies of the energy containing motions in the flow. These scales are well approximated in boundary layers using inner variables, where ν/u_τ is the estimate for the length of the smallest scales of motion, and u_τ^2/ν is the corresponding inner frequency.

2.1 Facilities

2.1.1 Melbourne Wind Tunnel

The Melbourne Wind Tunnel, formally called the High Reynolds Number Boundary Layer Wind Tunnel—HRNBLWT, has been used extensively since the mid-2000's. With test section dimensions of $\simeq$0.92 m × 1.89 m × 27 m, this facility reaches high Reynolds numbers with large corresponding viscous length scales $(\nu/u_\tau) \simeq 25\,\mu$m. (This value corresponds to the slowest speed needed to achieve $\delta^+ > 10,000$.) The contraction ratio of 6.2 along with the turbulent management section keeps the free-stream turbulence intensity $\leq$0.2 % throughout the entire working section. This facility is also housed in a laboratory, which keeps the fluid parameters constant for many hours. This enables especially long sampling durations. A schematic of the facility given by Kulandaivelu (2011), Talluru (2013), or de Silva (2014), and further details regarding the Melbourne Wind Tunnel are given in Nickels et al. (2005) and Nickels et al. (2007).

2.1.2 Flow physics facility

The FPF (phase I) became operational in 2011. In its present configuration, the FPF is an open circuit tunnel which draws and discharges air to atmosphere. The test section dimensions are $\simeq$2.8 m × 6 m × 72 m, with a maximum free-stream velocity of 14.5 m/s. This corresponds to a volume flow rate of 252 m^3/s. The phase I FPF does not feature a contraction, but uses a set of screens and honeycomb that maintain turbulent intensities between 0.2–0.5 %. Similar to that of the Melbourne Wind Tunnel, the FPF reaches high Reynolds numbers by employing a long development fetch. The viscous length scale for the lowest free-stream velocity that gives $\delta^+ > 10,000$ is $\simeq$70 μm. Additional information about this facility is given in Vincenti et al. (2013).

2.2 Mini-foss probe

The multi-element hot-wire probe used for acquisition of the present data is based on the design of Foss and Haw (1990). The probe consists of a vertical ×-array, with angles to the y-direction of nominally ±45°. This measures $\tilde{u}$ and $\tilde{v}$, where the tilde over a variable signifies an instantaneous quantity. The ×-array is accompanied by two single wires positioned parallel to the wall and perpendicular to the mean flow. These measure $\tilde{u}$. As shown in Fig. 1 the two parallel-array wires are woven in-between the top and bottom of the ×-array.

The spanwise vorticity fluctuations are given by the difference between two velocity gradients.

$$\omega_z = \frac{\partial v}{\partial x} - \frac{\partial u}{\partial y} \tag{2}$$

The time-average of $\tilde{\omega}_z$, $|\Omega_z|$, is well approximated by $\mathrm{d}U/\mathrm{d}y$, with $\mathrm{d}V/dx$ negligible under the boundary layer approximation. Here $\partial u/\partial y$ was calculated by taking the difference between u measured by the upper and lower

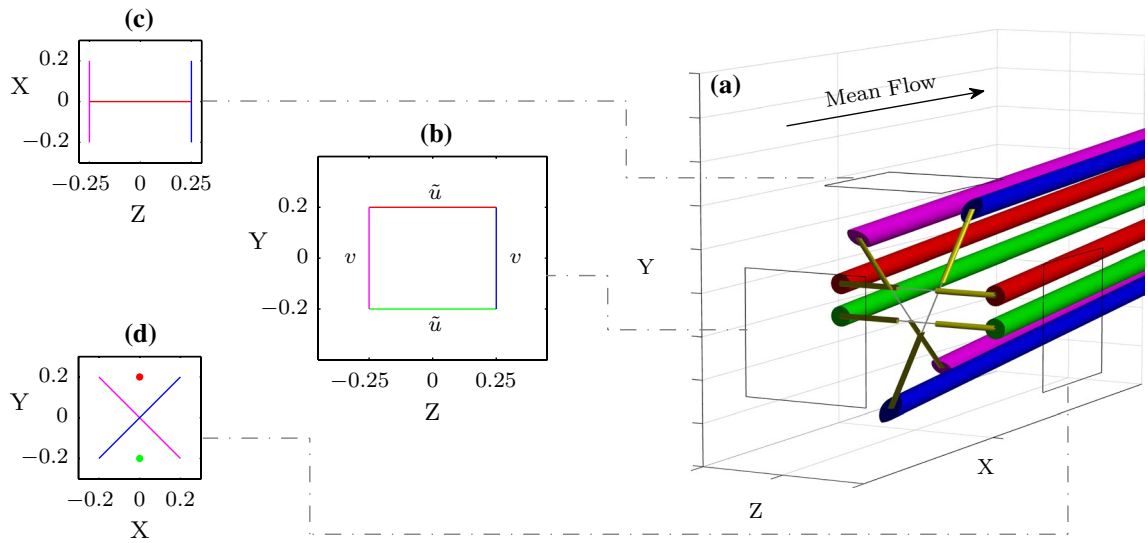

Fig. 1 Diagram of the mini-Foss probe. Units are in millimeters. **a** Illustration of probe. The colored cylinders represent the support prongs. Each color corresponds to a prong pair that holds an individual wire. **b** spanwise-wall-normal plain view of sensor configuration, colors correspond to prong pair. **d** spanwise-streamwise plain view of sensor configuration, colors correspond to prong pair. **c** streamwise-wall-normal plain view of sensor configuration, colors correspond to prong pair

parallel wires divided by the wall-normal distance between the wires ($\Delta y^+ \simeq \frac{4}{5} l^+$, where l is the axial length of the sensing element). The streamwise gradient, $\partial v/\partial x$, is estimated using Taylor's hypothesis, which transforms the time series into a streamwise spatial series. The spatial series was filtered so that $\partial x \approx \partial y$; again, a difference was taken and divided by the spacing. The spanwise spacing between the ×-array wires is $\Delta z^+ \approx l^+$ for the current experiments.

The sensing material was 2.5 µm diameter platinum-coated-tungsten wires with an active region of 500 µm in order to satisfy an $l/D \simeq 200$ (Ligrani and Bradshaw 1987). This wire was copper plated to a diameter ≈25 µm and soldered to the end of the prongs. A nitric acid solution was used to etch the copper plating from the portion of the wire that is used for sensing. Platinum-coated-tungsten is tungsten wire that is plated with a thin layer of platinum (∼8 % area), which protects the tungsten from corrosion and enhances the ability to solder to the wire. It was chosen over platinum due to its strength. The tensile strength of tungsten is about ten times greater than platinum, while they share approximately the same coefficient of resistivity, see Tropea et al. (2007). The trade-off of using tungsten is an increase in the thermal conductivity coefficient. Thermal conductivity influences end conduction of the hot-wire system, which negatively impacts the high frequency response (Khoo et al. 1998). Since the largest frequency needed to resolve the turbulent motions herein is relatively small, end conduction effects are minimal despite the choice of sensing material.

2.3 Calibration and processing

The calibration of the mini-Foss probe is a coupled two part process; the single wires and the ×-array.

2.3.1 Single wire

The parallel wires present on the probe act as typical single wire sensors. The electronic response of this type of wire is assumed to only be sensitive to the streamwise component of velocity in a unidirectional mean flow. These sensors are calibrated in-situ; the probe is traversed to the free-stream some distance above the boundary layer, and the wind tunnel speed is varied over the range of velocities expected in the experiment. From such data an E (voltage) versus U curve is generated, and a function is fit to the data. The fitting function is theoretically King's Law; however, a third- or fifth-order polynomial are commonly used, because they provide a better fit over the velocity range (Bruun 1995; Perry 1982). A third-order polynomial was chosen for this study because it is the lowest order polynomial that accurately captures the voltage response. The third and fifth order polynomial fits were indistinguishable for the present data.

Free-stream calibrations were performed immediately prior to and after the boundary layer traverse (profile). These will herein be referred to as pre- and post-calibrations. During the profile the hot-wire was traversed periodically to the free-stream to acquire one additional voltage versus velocity relationship—this practice is referred to as

free-stream checks. These checks provided a way of updating the calibration curve at each wall-normal location of the profile. A detailed description of this method can be found in Talluru et al. (2014). Free-stream checks were only carried out in the Melbourne Wind Tunnel. This is because the FPF boundary layer thickness can reach upwards of 1 m, which takes a relatively long time to traverse. Free-stream checks were thus not used in the FPF experiments due to time considerations over which the wires might drift or the tunnel conditions might change. In these cases at each wall-normal location, the pre- and post-calibrations were interpolated using the temperature distribution during the profile.

2.3.2 Cross-wire

An articulating compressed-air driven jet was used to calibrate the sensors that make up the ×-array. The jet was designed and manufactured at the University of New Hampshire (Ebner 2014) with a nozzle design similar to that used in Ong and Wallace (1996). The present jet has a circular nozzle with an exiting diameter of 30 mm and a contraction area ratio of 9:1. It was mounted on a frame with angular displacement capabilities, driven by stepper motors, allowing the jet to articulate in both the pitch and yaw directions. To calibrate the probe, the jet was placed in the streamwise direction with its exiting nozzle ~1 mm upstream of the probe's sensing area. The sensing area was in the center of the rotation of the jet in the irrotational portion of the flow exiting the nozzle. Calibration of the pressure drop through the jet nozzle against velocity was determined prior to experiments using a Pitot-static tube. The jet was articulated through a series of pitch angles, θ, in the streamwise-wall-normal plane. The velocity of the jet (U_{mag}) was held constant for each sweep of pitch angles, $-30^\circ \leq \theta \leq 30$. From this a table of U_{mag}, θ and the measured E_1 and E_2 was generated; here the subscripts that follow E are for wire 1 and wire 2 in the ×-array.

The topic of describing ×-array voltage response has been extensively covered over past half-century. The benefits and shortcomings of many methods are well documented (e.g., Bradshaw 1971; Perry 1982; Bruun 1995). The response of any hot-wire can be theoretically described using two equations: King's Law, and Jorgenson's expression (Jorgensen 1971, Eq. 3). The former relates the voltage response of a cylinder to the effective convective cooling velocity, and the latter is a decomposition of the cooling velocity into the cylinder's coordinate system. The most basic form of processing ×-array data is the cosine-law method (CLM), which assumes an angle between the wires (usually measured with a microscope). It further employs this angle to find an empirical relationship between the cooling of the wire and the flow angle. This can be extended to the effective angle method (EAM), which uses a single velocity full angle displacement calibration to find an *effective* angle between the wires based on their response to a change in angle (Bradshaw 1971).

Many researchers have found inadequacies in a single velocity full angle displacement schemes. Instead, they have conducted a full velocity range and angle displacement calibration. This method, called the look-up table technique (LUT), was first given by Willmarth and Bogar (1977). It maps each calibration voltage pair to each component of velocity present in the calibration. Examples of this mapping can be found in Johnson and Eckelmann (1984), Lueptow et al. (1988) and Abdel-Rahman et al. (1989). For the reconstruction of the velocity components, the LUT needs an interpolation scheme with a very finely spaced grid. These schemes assume a relationship between the calibrated velocities and flow angles. This is further discussed in Willmarth and Bogar (1977), Lueptow et al. (1988), Chew and Ha (1990), Vukoslavcevic et al. (1991), Osterlund (1999), Dijk and Nieuwstadt (2004) and Burattini and Antonia (2005). Burattini and Antonia (2005) also compared many ×-array calibration techniques and concluded that the LUT is more reliable than the EAM. However, most LUT schemes do not use the theoretical equations, but instead rely heavily on a "one-to-one" voltage pair to velocity relationship from the calibration. The issue that arises with this approach is when taking the gradient of the mapped surface. The gradient of the scheme directly influences the measured fluctuation (discussed further below); thus, the selection of a fit lacking theoretical basis can introduce large and intractable uncertainties into the probability density function of the velocity components, and the correlations that are subsequently measured.

The present approach adopts the philosophy that the angular response of the wires follow the Jorgenson's expression. Similarly to what was discussed in the *single wire calibration* the voltage response with increasing velocity does not have to abide by the theoretical relation since it is advantageous for this to be a bijective function and King's Law (or modified King's Law) does not provide the best fit.

Perry and Morrison (1971) introduced a dynamic calibration technique for single wires. The premise here is that the theoretical cooling equations are not adequate when the coefficient, K, describing the small perturbations from the calibration is determined statically. Perry and Morrison (1971) used a modified King's law approach to express $K = \partial E/\partial U = nBU^{n-1}/2E$, which is found using a Taylor series expansion of $\tilde{e}$. This was then expanded to cross-wires by Morrison et al. (1972). They postulated that a real hot-wire may experience wire bowing, departure from a cylinder cross sectional area, end conduction, and fluid variability associated with viscosity, density, and temperature.

To avoid these issues, they moved away from using the cooling equations and began to directly measure K by sinusoidally perturbing the wire (either with or perpendicular to the flow) at fixed mean velocities. When doing this, they reported that K changes from its static value. Conversely, Bruun (1995) found the difference between the static and dynamic approach to be negligible in determining K, if a modification to the cooling equation was made. It should be noted that Perry and Morrison (1971) and Morrison et al. (1972) a priori selected n values and looked for the best linear fit when plotting E^2 versus U^n. This way of calibrating has since been dismissed due to the ease of a computer-based search for the optimal fit. The present study did not perform a dynamic calibration and, therefore, cannot comment on its efficacy. However, using the Taylor expansion approach has the advantage of relating the voltage fluctuation to a velocity fluctuation absent of the mean flow. Doing this has two compelling advantages: voltage fluctuations are far less vulnerable to calibration drift than their mean counterpart; and in the mean the cooling due to V or W in boundary layers is negligible, and therefore, using these values to obtain fluctuations could be introducing large relative error.

2.3.3 Cross-wire: theoretical framework

The present four-element sensor acquires more information than a typical ×-array. The overall strategy of the ×-array calibration is to use this information to advantage. It is well established in the literature (Bruun 1995; Perry 1982) that the effective cooling velocity of a hot-wire (given by Jorgensen (1971)) can be written as,

$$\tilde{u}_e^2 = \tilde{u}_n^2 + k^2\tilde{u}_t^2 + h^2\tilde{u}_b^2 \tag{3}$$

Here, $\tilde{u}_e$ is the effective cooling velocity and $\tilde{u}_n$, $\tilde{u}_t$ and $\tilde{u}_b$ are the normal, tangential and bi-normal velocity components relative to the wire, respectively. The coefficients k and h are often referred to as the yaw and pitch coefficients. In Eq. 3 $\tilde{u}_n$, $\tilde{u}_t$, $\tilde{u}_b$ are unknowns and $\tilde{u}_e = f(\tilde{e})$ can be attained from any wire in the array, therefore, at least three wires are needed to solve the system of equations. However, due to the orientation of the ×-array, the cooling is insensitive to $\tilde{u}_b$ relative to $\tilde{u}_n$ and $\tilde{u}_t$ and is neglected in Eq. 3.

$$\tilde{u}_e^2 = \tilde{u}_n^2 + k^2\tilde{u}_t^2 \tag{4}$$

Note that this assumption only holds in nominally one- and two-dimensional flows (Perry 1982; Bruun 1995). Both Eqs. 3 and 4 are written with respect to the wire. In practice it is beneficial to have $\tilde{u}_e$ written in the same coordinate system as the flow,

$$\tilde{u}_e^2 = \tilde{u}_{\text{mag}}^2\left[\cos^2(\phi+\theta) + k^2\sin^2(\phi+\theta)\right] \tag{5}$$

Here θ is the incident angle of the flow relative to the flow coordinate system, and ϕ is the effective cooling angle. Since this wire configuration neglects the bi-normal velocity component, and in this study the probe is always aligned in the streamwise-wall-normal plane, $\tilde{u}_{\text{mag}}$ is taken to be a function of only streamwise and wall-normal of velocity ($=g(\tilde{u},\tilde{v})$).

$$\tilde{u}_e^2 = (\tilde{u}\cos\phi - \tilde{v}\sin\phi)^2 + k^2(\tilde{u}\sin\phi + \tilde{v}\cos\phi)^2 \tag{6}$$

or equivalently,

$$\tilde{u}_e^2 = \tilde{u}^2\left(\cos^2\phi + k^2\sin^2\phi\right) + \tilde{v}^2\left(\sin^2\phi + k^2\cos^2\phi\right) + \tilde{u}\tilde{v}\left(2k^2\cos\phi\sin\phi - 2\cos\phi\sin\phi\right) \tag{7}$$

The traditional application of the EAM assumes ϕ and k are independent of mean velocities. However, Snyder and Castro (1998) and Bakken and Krogstad (2004) report that ϕ is a function of mean velocity, and becomes more nonlinear at low velocities. Similarly, using an oscillating probe in a wind tunnel Lawson and Britter (1983) showed that k changes considerably for velocities between 0.3 and 3 m/s. From this it is assumed that both ϕ and k are functions of velocity, albeit relatively weak functions. Therefore, Eq. 7 combined with $\tilde{u}_e = f(\tilde{e})$ can be written as,

$$f(\tilde{e}) = \left[\tilde{u}^2L(U_{\text{mag}}) + \tilde{v}^2M(U_{\text{mag}}) + \tilde{u}\tilde{v}P(U_{\text{mag}})\right]^{1/2} \tag{8}$$

where L, M, and P are net functions of U_{mag}. As discussed previously, fluctuating components are traditionally found by computing the total velocity and subtracting the mean. For ×-arrays the sensitivity of V (or W if rotated 90°) is on the same order as the bi-normal component. Therefore, consistent with neglecting $\tilde{u}_b$ we also neglect V. This issue is not exclusive to hot-wire anemometry. PIV shares a similar problem, and due to the optimization of particle displacement in the streamwise component, sub-pixel algorithms are needed to measure any non-axial displacement (Adrian and Westerweel 2011). For this reason in any unidirectional mean flow, it is beneficial to calculate v independent of V.

A direct way to accomplish this involves expanding $\tilde{e}$ using a Taylor series in a manner similar to that used in the dynamic calibration approach by Morrison et al. (1972).

$$\tilde{e} - E = K_u u + K_v v + \frac{1}{2}\left[K_{uu}u^2 + 2K_{uv}uv + K_{vv}v^2\right] - \frac{1}{2}\left[K_{uu}\overline{u^2} + 2K_{uv}\overline{uv} + K_{vv}\overline{v^2}\right] \tag{9}$$

Here K signifies the partial derivative of $\tilde{e}$ with respect to the subscript evaluated at the operating point, and the number of subscripts denotes the order of the derivative. Equation 9 is only expanded to the second order as

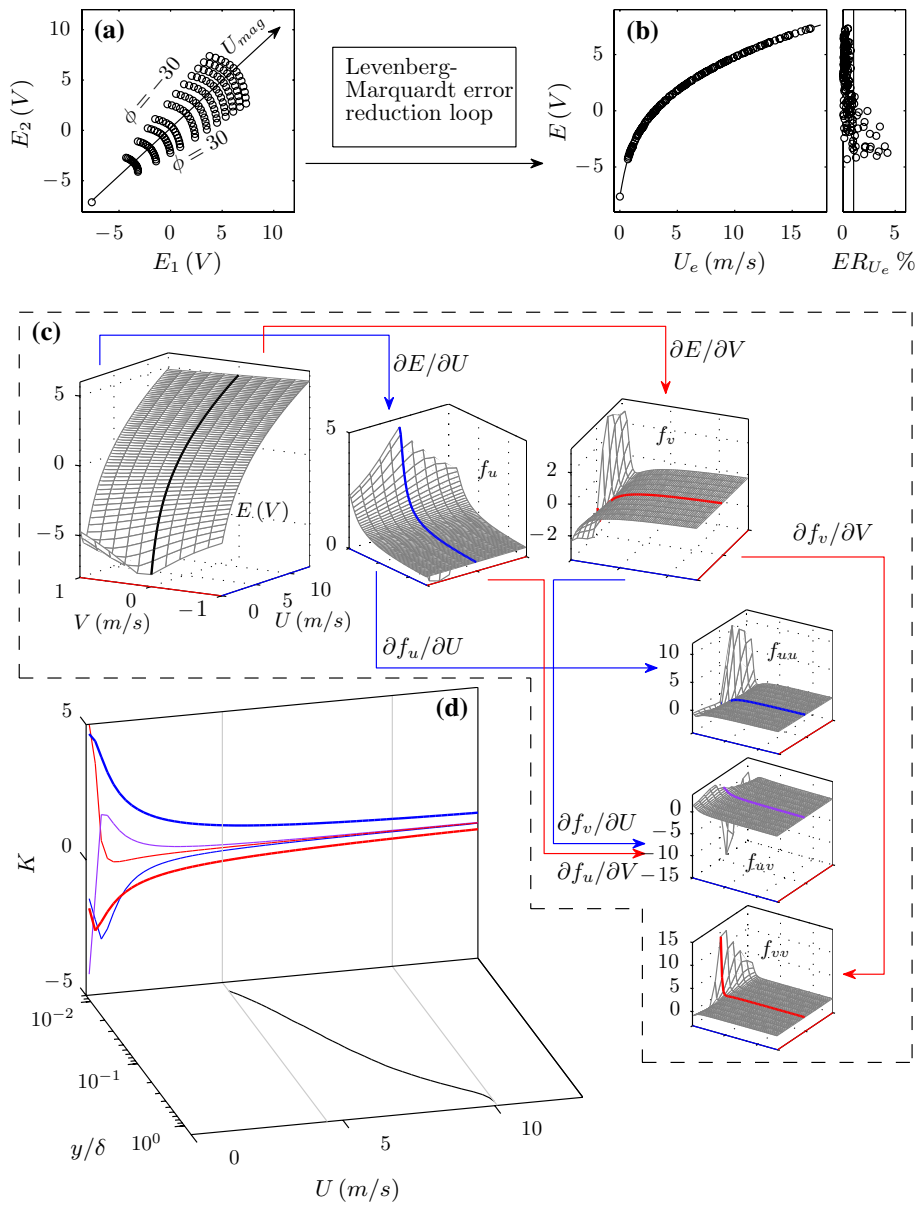

Fig. 2 Procedure to transform jet calibration data into the K coefficients found in Eq. 9. This procedure is carried out for each wire for every profile. **a** Typical voltage response for increasing angle and jet velocity. **b** Unique curve found by conducting the least-squares error loop to solve for $\phi(U)$, $k(U)$ and the polynomial coefficients present in Eq. 8. The goodness of the fit is plotted as a percent error in measured U_e. **c** Process of determining the voltage-velocity derivative of the relationship found in (**b**). *Blue* and *red arrows* represent derivatives with respect to U and V respectively. f is a corresponding surface of the derivative of E with respect to its subscript, the number of subscripts denotes the order of the derivative. The colored lines on the surface plots are the K values for that surface. **d** Plots the K coefficient versus the operating point U on the vertical plane. The lines are as follows: K_u ——, K_v ——, K_{uu} ——, K_{uv} ——, and K_{vv} ——. The *horizontal plane* projects U against the outer-normalized wall position. The *gray lines* bound the K values used in a profile

explained later, but importantly it is nonlinear. The operating point is the mean velocity at which the wire is being cooled $U_{\text{mag}} = (U^2 + V^2)^{1/2} \simeq U$. With this framework a practical calibration scheme was developed.

2.3.4 Cross-wire: practical calibration

Figure 2 shows a flow chart of the calibration processing procedure. After the voltage responses have been logged, subsequent the jet calibration (Fig. 2a), the polynomial coefficients (third order), ϕ and k are determined. This is accomplished by using Eq. 8 and employing a Levenberg-Marquardt nonlinear least squares algorithm. All the desired variables are found in one step, with the caveat that ϕ and k are constant for all U_{mag}. To satisfy the condition that ϕ and k are functions of U_{mag} at each calibration velocity, the same technique is employed but the polynomial coeffcients are held constant. Figure 2b shows the polynomial fit and U_e, along with the corresponding error of U_e relative to the fit. Only at effective velocities less than 5 m/s does the error exceed the black 1 % line. This derives primarily from imposing a single fit over the entire velocity range, rather than an effect of increased error at low velocities. For the low free-stream velocity profiles, when the velocity range is small, the error at lower U_e decreases. It should be noted that there are 156 calibration points and about 10 % exceed the 1 % error threshold.

The pre-calibration was solely used for processing the ×-array data. This is justified when making the assumption that small drift in hot-wires acts as a ΔE shift (Talluru et al. 2014). When this is the case, the gradient of the polynomial

between the pre- and post-calibrations is the same. The post-calibration is used only to confirm a ΔE drift. This is determined by solving for the U_e of the post-calibration using the $\phi(U)$ and $k(U)$ values of the pre-calibration, then fitting a polynomial. A maximum deviation of 1 %, between the gradients of the polynomial fits, from pre- to post-calibration was deemed permissible. Profiles with deviations exceeding this threshold were discarded. All the data presented abides by this criterion.

Using the polynomial coefficients, $L(U)$, $M(U)$, and $P(U)$ a surface is generated between U, V and E (Fig. 2c). This is accomplished by varying U and V by small increments over the expected range in the boundary layer, and solving for E at each grid point using Eq. 8. First- and second-order derivatives of E are taken with respect to both U and V. These derivative surfaces are evaluated at all potential operating points (i.e., over the full range of U and $V = 0$), yielding the $K(U)$ functions present in Eq. 9. Figure 2d plots $K(U)$ against the operating points.

2.3.5 Cross-wire processing

Cross-wire array processing employs Eq. 9. This equation is nonlinear, and there are three unknowns u, v and uv for each wire present, which renders it indeterminate. However, with known u it changes to an equation with a single unknown that can be solved iteratively. The present sensor benefits from having u information from the parallel array wires. Single element sensors are well-accepted to provided the most accurate measure of u than any other hot-wire configuration. This additional information allows temporal optimization of the v time series. The average of the parallel single wires at each instant is thus taken to be the corresponding velocity fluctuation at the measurement location of the ×-array (u_x). This is assumed to be valid since the inner-normalized wall-normal spacing between the sensors is ≤13.8 for all data sets and usually ≤10. The K values in Eq. 9 are a function of the operating point which changes at each wall-normal location. The operating point is taken to be the average between the parallel wire mean velocities, U_x. With this, the $K(U)$ curves can be interpolated at U_x to yield the specific K coefficients for each wall-normal location. The v time series can then be determined for each wire in the ×-array. Though Eq. 9 is nonlinear, there is only one real solution for each wire. An average of both real solutions is used to determine the final v time series.

When processing the data as an ×-array, it is apparent that each method yields detectably different statistical results, and especially so for $\overline{v^2}^+$ and $\overline{uv}^+$. Appendix 1 briefly addresses the complications of using a simple LUT method and provides comparisons to the present scheme. It should be noted that the present calibration and processing scheme should not be thought of as an ×-array method since each wire is treated separately. For ×-arrays, the unique relationship between the wires is needed to determine both $\tilde{u}$ and $\tilde{v}$ simultaneously. The quality of the calibration and assumed response between calibration points, dictates the total combined cooling allocated to $\tilde{u}$ and $\tilde{v}$. In the present scheme u is an input, which results in the remainder of the cooling response fluctuation (for one wire) being a function of v. Note that this is still calibration dependent. However, the velocities are not being solved for in parallel (like in a LUT based method), and only v is determined instead of $\tilde{v}$.

3 Results

The experimental parameters are presented in Table 1. There are a total of seventeen profiles ranging in δ^+ from ~2000–12,700. To be consistent with previous publications from the authors $\delta^+ = \delta_{99}u_\tau/\nu$ and $Re_\tau = \delta_c u_\tau/\nu$, where the subscript c indicates the "composite" fit given by Chauhan et al. (2009). Since the wall-normal locations for each profile were logarithmically spaced the "composite" fit was used to determine δ_{99}. This provides a more consistent option than the alternative of using some type of interpolation scheme. The ratio Re_τ/δ^+ is given and shows that on average, for this data, δ_c is ~25 % larger than δ_{99}. At constant Π values (wake parameter), this ratio should be fixed. Differing Π values is thought to be the main cause of the variation; however, the profiles are logarithmically spaced so any representation of δ is an approximate estimate. There are five different symbols used to represent the profiles. Each symbol corresponds to a spatial resolution range; e.g., the circles indicate that $8 \leq l^+ < 10$. The symbols are use a sequential colored scheme based on the Reynolds number. For clarity only seven profiles were selected in the presentation of mean statistics. These profiles are denoted with a check mark next to the facility acronym. They represent the entire range in Reynolds number and include profiles from both the Melbourne Wind Tunnel and the FPF.

3.1 Mean statistics

Inner-normalized mean velocity profiles are plotted in Fig. 3. The friction velocity u_τ was determined by applying the "composite fit" given by Chauhan et al. (2009), and employing $\kappa = 0.39$ and $A = 4.3$ given by Marusic et al. (2013). The data taken at the FPF show good agreement with that from the Melbourne Wind Tunnel, with all exhibiting consistent δ^+ trends. Recent works of Woodcock and Marusic (2015) and Klewicki et al. (2014) give evidence that the inverse of the leading order coefficient in the logarithmic law approaches a constant value with increasing δ^+. Therefore, the u_τ values, estimated using this method, are

Table 1 Properties of the boundary layers examined herein

Symbol	δ^+	Re_τ/δ^+	U_∞ (m/s)	u_τ (m/s)	ν/u_τ ($\times 10^{-6}$ m)	l^+, Δz^+	Δy^+	$f_s(\times 10^3\ 1/s)$	TU_∞/δ_{99}	x (m)	Facility
△	1951	1.25	10.1	0.368	43.4	11.5	9.4	30	85450	4.5	✓ HRNBLWT
△	2622	1.24	10.1	0.356	45.2	11.1	9.1	30	25681	7.0	HRNBLWT
□	2711	1.26	4.4	0.156	94.9	5.3	4.7	25	4091	16.0	✓ FPF
▷	2928	1.27	15.2	0.541	29.6	16.9	13.8	30	105131	4.5	✓ HRNBLWT
◇	3588	1.27	6.6	0.230	66.8	7.5	6.7	25	6619	16.0	FPF
▷	3770	1.26	15.1	0.519	30.6	16.3	13.4	30	39342	7.0	HRNBLWT
△	3844	1.24	10.0	0.340	46.8	10.7	8.8	30	40241	11.9	✓ HRNBLWT
○	4245	1.27	8.8	0.301	51.9	9.6	8.7	25	9560	16.0	FPF
□	4739	1.28	4.2	0.144	100.2	5.0	4.5	25	2660	34.1	FPF
△	5593	1.26	10.0	0.334	47.8	10.5	8.6	30	22517	18.0	✓ HRNBLWT
◆	6061	1.27	6.6	0.220	68.1	7.3	6.6	25	4773	33.9	FPF
▶	6080	1.28	15.3	0.512	30.7	16.3	13.4	30	24539	11.9	HRNBLWT
■	7386	1.28	4.3	0.144	107.5	4.7	4.2	25	1639	66.1	FPF
●	7486	1.29	8.8	0.293	52.9	9.4	8.5	25	6658	34.0	FPF
▶	7894	1.27	15.3	0.497	32.1	15.6	12.8	30	54353	18.0	✓ HRNBLWT
◆	10075	1.30	6.6	0.215	70.7	7.1	6.4	25	2762	66.0	FPF
●	12509	1.31	8.8	0.285	55.0	9.1	8.2	25	3826	66.0	✓ FPF

The check mark denotes the primary data sets that are shown in Figs. 3, 4, 5, 8, 11, and 10

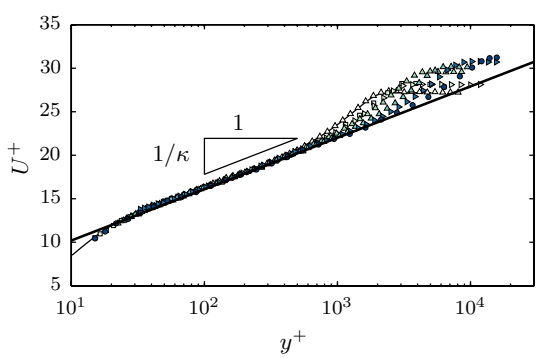

Fig. 3 Mean velocity profile normalized by inner variable. The *solid black line* is $U^+ = 0.39^{-1}\log(y^+) + 4.3$ (Marusic et al. 2013). Symbols are given in Table 1. The *black* comparison profile is Sillero et al. (2013) DNS $\delta^+ \approx 2000$

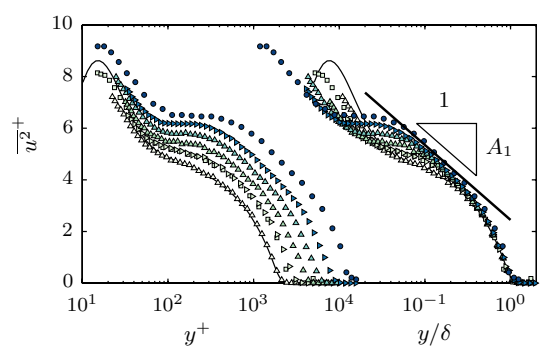

Fig. 4 Inner-normalized streamwise velocity variance plotted with respect to inner- and outer-normalized wall position. The *black solid line* is the logarithmic decay given by the attached eddy hypothesis (Townsend 1976) and $A_1 = 1.26$ (Marusic et al. 2013). Symbols are given in Table 1. The *black* comparison profile is Sillero et al. (2013) DNS $\delta^+ \approx 2000$

expected to become more accurate with increasing δ^+. The lowest δ^+ profile presented, is at approximately the same δ^+ as the DNS of Sillero et al. (2013), and show good agreement throughout the flow. Therefore, the κ and A values are deemed appropriate for the present δ^+ range.

Profiles of inner-normalized streamwise velocity variance are plotted against inner- and outer-normalized wall position in Fig. 4. Comparison with the DNS shows excellent agreement for $y^+ \geq 80$. Interior to this position the hot-wire data exhibits a small attenuation. This is because the energetic signature in this region is due to the viscous-scaled near-wall motion (Kline et al. 1967) which are being spatially averaged even with an $l^+ \approx 10$. With increasing δ^+ these near-wall motions increase in energy resulting in a larger inner peak in $\overline{u^2}^+$ (Klewicki and Falco 1990; DeGraaff and Eaton 2000; Metzger and Klewicki 2001; Hutchins et al. 2009; Vincenti et al. 2013). At the FPF the present probe was able to traverse to the inner peak. Here the near-wall trend for this profile follows the expected δ^+ behavior. Hutchins et al. (2009) cautions concluding on inner-peak growth when the spatial resolution is changing. The profiles presented herein all belong to "development" sets (approximately constant l^+); i.e., the free-stream is held constant and δ^+ is increased with increasing streamwise position. There are a total of five "development" sets

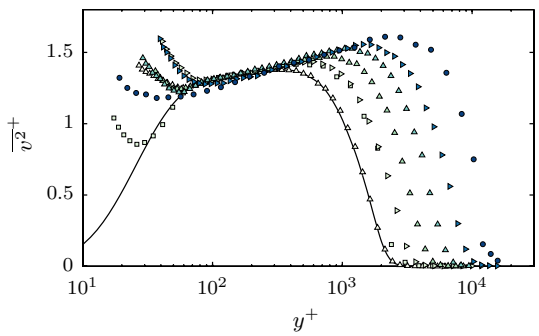

Fig. 5 Inner-normalized wall-normal velocity variance profile. Symbols are given in Table 1. The *black* comparison profile is Sillero et al. (2013) DNS $\delta^+ \approx 2000$

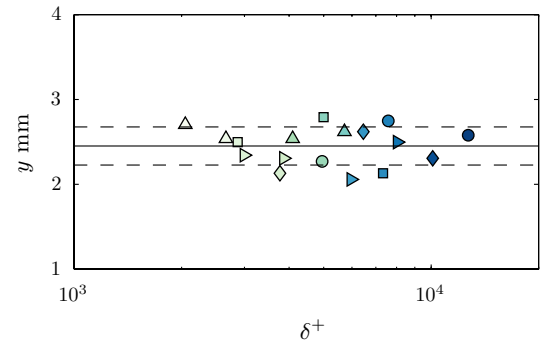

Fig. 6 Physical wall-ward location when $\overline{v^2}^+$ begins the artificial near-wall increase. Symbols are given in Table 1. *Solid black line* is the mean wall location of increase, and the *black dashed lines* represent ± 1 standard deviation

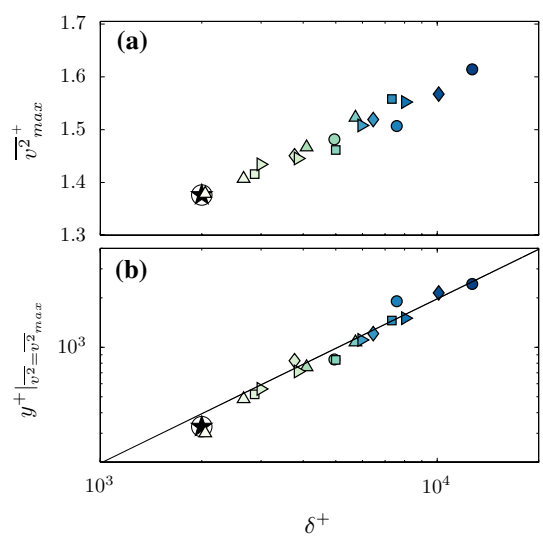

Fig. 7 Outer peak magnitude of the wall-normal velocity variance is given in (**a**) and the corresponding inner-normalized wall location is plotted in (**b**). Both are versus Reynolds number. Symbols are given in Table 1. The *black fit line* in (**b**) is $0.2\delta^+$. The ⊛ comparison point is Sillero et al. (2013) DNS $\delta^+ \approx 2000$

with at least three streamwise positions (or δ^+) in each set. The observation of inner-peak growth with δ^+ is made when considering profiles of constant l^+ and is observed for each of the three "development" sets (9 profiles) where the probe was traversed to the inner-peak. Note that all profiles considered for this observation had a sensor size of $l^+ < 10$. Profiles for $\delta^+ > 6000$ show evidence of an emerging plateau region. This plateau starts beyond the decay in the near-wall peak. Outer-ward of the plateau the profile exhibits an approximately logarithmic decrease. Empirical evidence indicates the start of the logarithmic decrease begins at $y^+ = C(\delta^+)^{1/2}$, where C is an $\mathcal{O}(1)$ constant, Marusic et al. (2013), Vincenti et al. (2013). $C = 2.6$ is consistent with the inertial leading mean dynamics (Klewicki 2013), while Marusic et al. (2013) conservatively use $C \cong 3$. Consistent with the notion of Townsend (1976), the logarithmic regions for the mean and variance are the same, and thus extend to $y/\delta \sim 0.2$. It should be noted that Marusic et al. (2013) uses Re_τ which as indicated is always larger than δ^+. Therefore, $3(Re_\tau)^{1/2} \approx 3.4(\delta^+)^{1/2}$ and the outer-bound of $\sim 0.2\delta^+ \approx 0.15 Re_\tau$. The outer-normalized profiles merge, and this is consistent with Townsend's Reynolds number similarity hypothesis (Townsend 1976). The decaying logarithmic slope given by Marusic et al. (2013) is shown for the highest δ^+ profile.

Figure 5 plots the inner-normalized wall-normal variance. The $\delta^+ \simeq 2000$ profile shows good agreement with the DNS profile for $y^+ \geq 80$, but interior to this point trends upwards. This behavior is noticed in all the profiles, but not at a consistent inner-normalized wall position. The profile with the best spatial resolution ($\delta^+ = 2754$) agrees with the near-wall DNS until about $y^+ \approx 30$. It is also noticed that the deviation moves outward in viscous units with increasing l^+. Figure 6 shows the wall positions in physical units where the profiles first merge with the DNS for all of the data presented. The cause of the increased (near wall) wall-normal velocity intensity is unclear, but over the present δ^+ range it seems to correlate with physical distance from the wall. Hot-wires are intrusive, and the flow needs to circumvent the probe. The assumption is that this effect is included in the calibration, which in the present case is static (mean calibration). If there was probe blockage, there would be lower momentum fluid farther from the wall than anticipated which would manifest in the mean flow. In the present data the mean flow shows typical behavior. Also, $\overline{u^2}^+$ does not show abnormal characteristics, indicating that the single parallel wires are not being affected. For $\overline{v^2}^+$ to increase, when the probe is in close proximity to the wall, the cooling of the ×-array wires must be artificially stimulated. From this, the instantaneous flow angles might experience a slight magnification when the probe

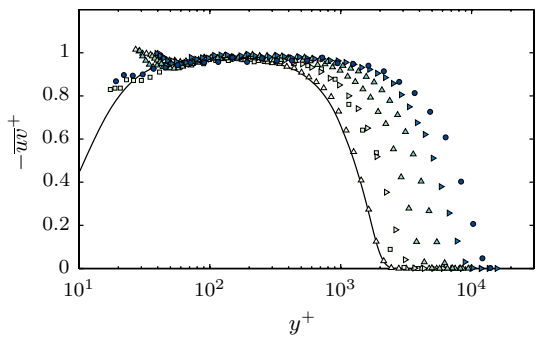

Fig. 8 Inner-normalized Reynolds stress profile. Symbols are given in Table 1. The *black* comparison profile is Sillero et al. (2013) DNS $\delta^+ \approx 2000$

confines the flow near the wall. This appears to be a different effect than the flow being swept upward. The average wall position of the "peel-up" (y_{pu}) is approximately 25 % greater than the wall-normal dimension of the probe. Between $y^+_{pu} \leq y^+ \leq 100$ all profiles reasonably agree with the DNS. At $y^+ \approx 0.2\delta^+$ each profile reaches a maximum and then decays to zero near δ. The profile maxima increase with increasing δ^+.

The peak magnitude in the wall-normal velocity variance with respect to δ^+ is given in 7(a), with its corresponding inner-normalized wall-normal location given in 7(b). For consistency, and to reduce scatter, a fourth-order polynomial was fit over the profile values that exceeded 90 % of the maximum. The peak value in the fit determined the wall-normal location and the magnitude plotted in 7. The attached eddy model predicts, in the asymptotic limit, that the peak value plateaus (Perry and Chong 1982; Townsend 1976). Kunkel and Marusic (2006) provide a formulation of wall-normal variance, consistent with attached eddy arguments, which shows plateauing behavior at appreciably larger δ^+ than what is presented here and, therefore, the increase is consistent for this Reynolds number range. The black fit line in 7(b) is $y^+ = 0.2\delta^+$, suggesting that the location of the peak scales with Reynolds number and nominally resides at the upper end of the log-region.

The inner-normalized Reynolds stress ($\overline{uv}^+$) is shown in Fig. 8. The near-wall peel-up shown in $\overline{v^2}^+$ is manifest in the correlation of v with u, but the effect is not as severe. The agreement with the DNS is good beyond y^+_{pu}. Though subtle, the profiles show good agreement with expected peak location scaling with $\delta^{+1/2}$ (Sreenivasan 1989), and with the magnitude of the peak approaching u_τ^2 with increasing δ^+ (Townsend 1976). These attributes are more apparent in Fig. 9, where the Reynold stress gradient (turbulent inertia, $TI = -\partial\overline{uv}^+/\partial y^+$) is plotted versus wall-distance over the geometric mean of the bounding scales. The inset in Fig. 9 plots the peak value in $\overline{uv}^+$ (for $y^+ > 100$ to avoid peel-up) with Reynolds number. Although there is

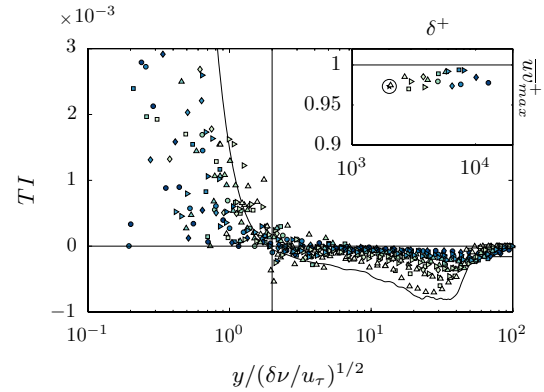

Fig. 9 Inner-normalized Reynolds stress gradient profiles. The inset is the maximum value of the inner-normalized Reynolds stress against Reynolds number. Symbols are given in Table 1. The *black* comparison profile in the main plot and the ⊛ point in the inset is Sillero et al. (2013) DNS $\delta^+ \approx 2000$

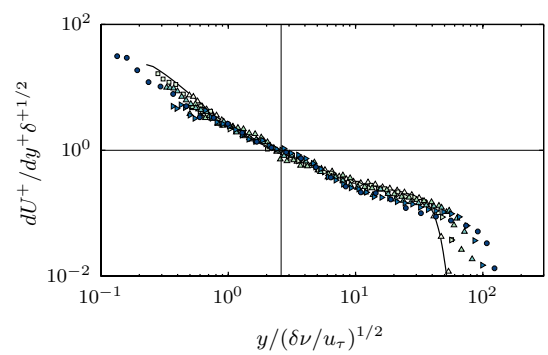

Fig. 10 Mean vorticity profiles normalized by the intermediate length scale $(\delta\nu/u_\tau)^{1/2}$. *Vertical line* denotes the onset of Layer IV. Symbols are given in Table 1. The *black* comparison profile is Sillero et al. (2013) DNS $\delta^+ \approx 2000$

scatter, these data agree with both the peak location prediction, and the trend toward the asymptotic value.

3.2 Spanwise vorticity structure

The capability of the present probe to measure $\tilde{\omega}_z$ is evaluated in two ways: the comparison of scaled Ω_z to theoretical predictions; and a rational Reynolds number trend in ω'_z. Scaling analysis of the MMB indicates that the gradient of the mean velocity profile $-\Omega_z = \mathcal{O}[u_\tau/(\delta\nu/u_\tau)^{1/2}]$ at $y = \mathcal{O}[(\delta\nu/u_\tau)^{1/2}]$ (Fife et al. 2005). Therefore, normalizing the respective quantities by the scales should cause all the profiles to merge at that location. Klewicki (2013) provides an extensive analysis of pipe, channel and boundary layers showing that at $y^+ = 2.6(\delta^+)^{1/2}$, $-\Omega_z^+(\delta^+)^{1/2} \approx 1$. This finding was later supported by Vincenti et al. (2013). Figure 10 agrees with this finding. Klewicki et al. (2009)

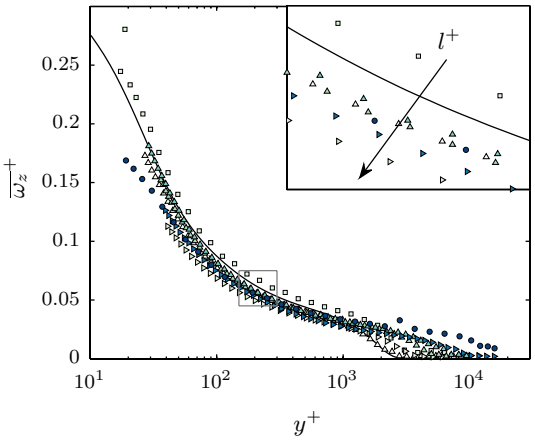

Fig. 11 Inner-normalized spanwise vorticity standard deviation. Symbols are given in Table 1. The *black* comparison profile is Sillero et al. (2013) DNS $\delta^+ \approx 2000$

analytically deduced that the inertial region begins near $y^+ = 2.6(\delta^+)^{1/2}$. This is consistent with the empirical findings of Marusic et al. (2013) that the log-region begins at $y^+ = 3(Re_\tau)^{1/2}$. Figure 10 plots $-\Omega_z$ against wall position with the indicated scaling. As is apparent, all the profiles pass through unity at the expected location.

Figure 11 plots the standard deviation of the spanwise vorticity normalized by inner variables. The comparison with the DNS shows good agreement, but the hot-wire profile is slightly attenuated. This is an expected result for the given spatial resolution. The sensor spacing of the parallel wires is given in Table 1 as Δy^+, and is approximately 80 % of l^+. This is a key parameter in the accurate estimation of ω_z. Wallace and Foss (1995) provide an extensive discussion of the issues associated with this spacing. They report that when $\Delta y \lesssim 2\eta$ (where $\eta = (\nu^3/\epsilon)^{1/4}$ is the Kolmogoroff microscale, and ϵ is the turbulent dissipation) the u signals may be too similar and $\Delta u/\Delta y$ is largely the difference of noise. However, with increasing $\Delta y/\eta$ spatial attenuation will occur due to the small scale nature of the ω_z motions. Morrill-Winter and Klewicki (2013) provide evidence that the characteristic length scale (peak wavelength) of the vorticity is $\mathcal{O}[(\delta\nu/u_\tau)^{1/2}]$ for the entirety of the boundary layer for $375 \leq \delta^+ \leq 8.9 \times 10^5$. Therefore, approximately consistent attenuation is expected for the measured $\overline{\omega_z}^+$ for the entire profile at a fixed Δy^+. The inset of Fig. 11 shows a small subset of the overall profile to emphasize the spatial resolution effect. There is one profile that sits above the DNS. For this profile $\Delta y = 4.7\nu/u_\tau \approx 1.5\eta$ (assuming $3\nu/u_\tau \sim \eta$, approximate near the wall—see Klewicki and Falco (1990) and Kulandaivelu (2011)), which is consistent with the noise amplification described. The standard deviation of ω_z at the wall is maximum and with increasing wall position decreases. It is observe that the profiles look similar for all the Reynolds numbers presented here, and they appear to follow the same decreasing curve (albeit with slight spatial attenuation for the larger l^+ profiles). Due to the boundary condition, and the defining characteristic of the turbulence, $\overline{\omega_z}^+ = 0$ outside the boundary layer. Therefore, if there were a 'similar curve' for all Reynolds numbers, then at each δ^+ the $\overline{\omega_z}^+$ profile would have to deviate from this curve and decrease to zero. This departure location is empirically observed to be $y/\delta \approx 1/2$. If there are any subtle differences, they are masked by experimental uncertainty and spatial averaging effects.

4 Conclusions

Measurements of spanwise vorticity were acquired in turbulent boundary layers over a range of $1982 \leq \delta^+ \leq 12,697$. The measurements were obtained at low speeds allowing the data to be well resolved spatially and temporally with sensor dimensions of about 0.5 mm. Owing to the large flow development lengths afforded by the FPF (72 m) and Melbourne Wind Tunnel (27 m), high Reynolds numbers are attained by increasing x instead of U_∞. A custom probe was built for these measurements. It was based on the design of Foss and Haw (1990). An important feature of this probe is that all its sensing elements provide an average evaluation location at the same point, allowing gradients to be taken about that point.

A custom calibration and processing procedure was created to take full advantage of the flow velocity information provided by the sensor's four wires. This procedure calculates the wall-normal velocity fluctuation absent its mean and utilizes the theoretical angular displacement response given by Jorgensen (1971). This allows for both the effective cooling angle and pitch coefficient to change with local velocity. This, in turn, allows the v signal to be temporally optimized using the u component measurements from the parallel array.

The present results agree with the onset of the logarithmic region scaling with the geometric mean of the scale separation in the flow (Klewicki et al. 2009; Marusic et al. 2013). The streamwise variance profiles show support for Reynolds number similarity with a logarithmic decay that is well described by $A_1 \approx 1.26$ (Marusic et al. 2013). The wall-normal velocity variance exhibits a convincing δ^+ trend that is similar to that given by Kunkel and Marusic (2006). This includes a universal near-wall profile, and with increasing δ^+ the outer peak, located at $y^+ \approx 0.2\delta^+$, increases. The Reynolds stress approaches a maximum of u_τ^2 with increasing δ^+, and the Reynolds stress gradient exhibits a zero crossing consistent with the scaling given by Sreenivasan (1989) and the analysis of Wei et al. (2005). When normalized by the intermediate scale $(\delta^+)^{1/2}$

the mean spanwise vorticity passes through unity for all δ^+, where the mean dynamics become wholly inertial, see Klewicki (2013) and Vincenti et al. (2013). The inner-normalized spanwise vorticity r.m.s. profiles show a distinct δ^+ trend. These profiles nominally merge in the near-wall region, and following the same decreasing trajectory until $y/\delta \simeq 1/2$, where they exhibit a more severe descent to zero in the free-stream.

Acknowledgments The authors wish to gratefully thank the financial support of the Australian Research Council and the USA Office of Naval Research.

Appendix: Comparison of ×-array data processing methods

Sensor drift is a major challenge when processing ×-array data. In most methods, such as look-up tables (LUT) the processing scheme depends on a unique relationship between the wire voltage. If wire drift is experienced, this relationship becomes unknown, and in general is impossible to rectify without performing a new calibration. Conversely, for a single wire normal to the flow, drift can be accounted for if the drift is in the form of a DC-offset (ΔE-drift)—see Talluru et al. (2014). To account for sensor drift in ×-arrays, an interpolation between the pre- and post-calibration is usually preformed (commonly linear with time or based on the temperature history). Inherently, this assumes the rate of response change for each wire. In thermally stable environments, sensors usually experience response changes differently making a simple interpolation a poor estimate of the unique relationship between the wires. In the present processing method, the ×-array sensors are considered separately and a relationship between the sensors is never needed. Since the processing scheme only uses voltage fluctuations ΔE-drift is not present; i.e., the drift is removed as long as it is treated as a voltage shift. In fact, only profiles that were well-modeled by ΔE-drift were considered. Therefore, the only drift that needs to be considered is that of the single parallel wires.

The LUT method is commonly found in the literature as a processing method for ×-arrays (Chew and Ha 1990; Bakken and Krogstad 2004; Burattini and Antonia 2005; Ebner 2014). The $\delta^+ \simeq 1,951$ and $\delta^+ \simeq 7,894$ ×-array data were processed with the present method and the LUT. For this comparison, the LUT surface was generated from the calibration using a modified ridge estimator ("gridfit" command in Matlab), and a linear interpolation was performed between the pre- and post-calibration. Figures 12 and 13 compare the wall-normal velocity variance and

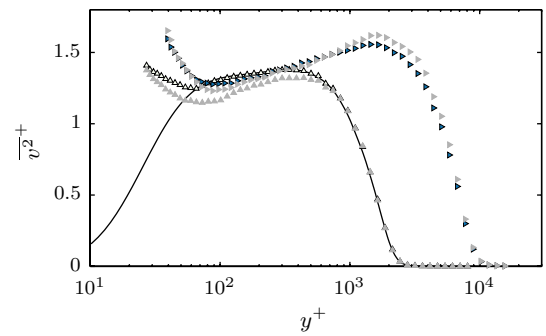

Fig. 12 Inner-normalized wall-normal velocity variance profile. Symbols are given in Table 1, and when a symbol is gray, it was processed with the LUT method. The *black* comparison profile is Sillero et al. (2013) DNS $\delta^+ \approx 2000$

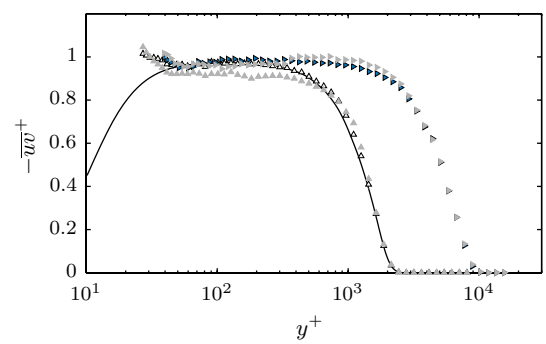

Fig. 13 Inner-normalized Reynolds stress profile. Symbols are given in Table 1, and when a symbol is gray it was processed with the LUT method. The *black* comparison profile is Sillero et al. (2013) DNS $\delta^+ \approx 2000$

the Reynolds stress profiles. It is clear from both figures that profiles processed with the LUT show less consistent behavior between the two Reynolds numbers considered. Also, the LUT profile at $\delta^+ \simeq 1951$ does not show the same level of agreement with the DNS as the present method. Peel-up is present in both methods suggesting that this phenomena is not a result of the processing scheme. These results provide evidence that the present method is more robust for these statistics. Note that the r.m.s. of vorticity was not considered here, since only a small percentage of its magnitude can be attributed to $\partial v/\partial x$ and becomes less so with increasing wall-normal position.

References

Abdel-Rahman AA, Hitchman GJ, Slawson PR, Strong AB (1989) An X-array hot-wire technique for heated turbulent flows of low velocity. J Phys E Sci Instrum 22(8):638

Adrian RJ, Westerweel J (2011) Particle image velocimetry. Cambridge University Press, Cambridge

Bakken OM, Krogstad P (2004) A velocity dependent effective angle method for calibration of X-probes at low velocities. Exp Fluids 37:146–152

Bradshaw P (1971) An introduction to turbulence and its measurement. Pergamon Press, Oxford

Bruun HH (1995) Hot wire anemometry: principles and signal analysis. Oxford University Press, Oxford

Burattini P, Antonia RA (2005) The effect of different X-wire calibration schemes on some turbulence statistics. Exp Fluids 38(1):80–89

Chauhan KA, Monkewitz PA, Nagib HM (2009) Criteria for assessing experiments in zero pressure gradient boundary layers. Fluid Dyn Res 41(2):021404

Chew YT, Ha SM (1990) A critical evaluation of the explicit data analysis algorithm for a crossed wire anemometer in highly turbulent isotropic flow. Meas Sci Technol 1(8):775

Chin C, Philip J, Klewicki JC, Ooi A, Marusic I (2014) Reynolds-number-dependent turbulent inertia and onset of log region in pipe flows. J Fluid Mech 757:747–769

de Silva CM (2014) Large-scale PIV measurements at high Reynolds numbers in wall-bounded turbulence. PhD thesis, University of Melbourne

DeGraaff D, Eaton J (2000) Reynolds-number scaling of the flat-plate turbulent boundary layer. J Fluid Mech 422:319–346

Ebner R (2014) Influences of Roughness on the Inertial Mechanism of Turbulent Boundary-Layer Scale Separation. Ph.D. thesis, University of New Hampshire

Fife P, Klewicki J, McMurtry P, Wei T (2005) Multiscaling in the presence of indeterminancy: wall-induced turbulence. Multiscale Model Simul 4:936

Folz A, James M (2010) Wallace. Near-surface turbulence in the atmospheric boundary layer. Phys D Nonlinear Phenom 239(14):1305–1317

Foss JF, Haw RC (1990) Transverse vorticity measurements using a compact array of four sensors, vol 97. In: Symposium on Thermal Anemometry, ASME FED

Hinze J (1975) Turbulence. McGraw-Hill, New York

Hutchins N, Nickels TB, Marusic I, Chong MS (2009) Hot-wire spatial resolution issues in wall-bounded turbulence. J Fluid Mech 635:103–136

Johnson FD, Eckelmann H (1984) A variable angle method of calibration for X-probes applied to wall-bounded turbulent shear flow. Exp Fluids 2(3):121–130

Jorgensen FE (1971) Directional sensitivity of wire and fiber-film probes. DISA Inf 11(3):1–7

Khoo BC, Chew YT, Lim CP, Teo CJ (1998) Dynamic response of a hot-wire anemometer. part i: a marginally elevated hot-wire probe for near-wall velocity measurements. Meas Sci Technol 9(5):751

Klewicki JC (2013) A description of turbulent wall-flow vorticity consistent with mean dynamics. J Fluid Mech 737:176–204

Klewicki JC, Falco RE (1990) On accurately measuring statistics associated with small-scale structure in turbulent boundary layers using hot-wire probes. J Fluid Mech 219:119–142

Klewicki JC, Fife P, Wei T (2009) On the logarithmic mean profile. J Fluid Mech 638:73–93

Klewicki JC, Philip J, Marusic I, Chauhan K, Morrill-Winter C (2014) Self-similarity in the inertial region of wall turbulence. Phys Rev E 90(6):063015

Kline SJ, Reynolds WC, Schraub FA, Runstadler PW (1967) The structure of turbulent boundary layers. J Fluid Mech 30(04):741–773

Kulandaivelu V (2011) Evolution and structure of zero pressure gradient turbulent boundary layer. Ph.D. thesis, University of Melbourne

Kunkel GJ, Marusic I (2006) Study of the near-wall-turbulent region of the high-Reynolds-number boundary layer using an atmospheric flow. J Fluid Mech 548:375–402

Lawson RE, Britter RE (1983) A note on the measurement of transverse velocity fluctuations with heated cylindrical sensors at small mean velocities. J Phys E Sci Instrum 16(6):563

Ligrani PM, Bradshaw P (1987) Spatial resolution and measurement of turbulence in the viscous sublayer using subminiature hot-wire probes. Exp Fluids 5(6):407–417

Lueptow RM, Breuer KS, Haritonidis JH (1988) Computer-aided calibration of X-probes using a look-up table. Exp Fluids 6(2):115–118

Marusic I, Monty J, Hultmark M, Smits A (2013) On the logarithmic region in wall turbulence. J Fluid Mech 716:R3

Metzger MM, Klewicki JC (2001) A comparative study of near-wall turbulence in high and low Reynolds number boundary layers. Phys Fluids (1994-present) 13(3):692–701

Morrill-Winter C, Klewicki J (2013) Influences of boundary layer scale separation on the vorticity transport contribution to turbulent inertia. Phys Fluids 25

Morrison GL, Perry AE, Samuel AE (1972) Dynamic calibration of inclined and crossed hot wires. J Fluid Mech 52(03):465–474

Nickels TB, Marusic I, Hafez S, Chong MS (2005) Evidence of the k_1^{-1} law in a high-reynolds-number turbulent boundary layer. Phys Rev Lett 95(7):074501

Nickels TB, Marusic I, Hafez S, Hutchins N, Chong MS (2007) Some predictions of the attached eddy model for a high reynolds number boundary layer. Philos Trans R Soc A Math Phys Eng Sci 365(1852):807–822

Ong L, Wallace J (1996) The velocity field of the turbulent very near wake of a circular cylinder. Exp Fluids 20(6):441–453

Osterlund JM (1999) Experimental studies of zero pressure-gradient turbulent boundary-layer flow. Ph.D. thesis, Royal Institute of Technology, Stockholm, Sweden

Perry AE (1982) Hot wire anemometry. Clarendon Press, UK

Perry AE, Morrison GL (1971) Static and dynamic calibrations of constant-temperature hot-wire systems. J Fluid Mech 47(04):765–777

Perry AE, Chong MS (1982) On the mechanisms of wall turbulence. J Fluid Mech 119:173–217

Priyadarshana PJA, Klewicki JC, Treat S, Foss JF (2007) Statistical structure of turbulent-boundary-layer velocity-vorticity products at high and low Reynolds numbers. J Fluid Mech 570:307–346

Sillero JA, Jiménez J, Moser RD (2013) One-point statistics for turbulent wall-bounded flows at Reynolds numbers up to $\delta^+ \approx 2000$. Phys Fluids (1994-present) 25(10):105102

Snyder WH, Castro IP (1998) The yaw response of hot-wire probes at ultra-low wind speeds. Meas Sci Technol 9(9):1531

Sreenivasan KR (1989) The turbulent boundary layer. In: Frontiers in experimental fluid mechanics. Springer, Berlin

Talluru KM, Kulandaivelu V, Hutchins N, Marusic I (2014) A calibration technique to correct sensor drift issues in hot-wire anemometry. Meas Sci Technol 25(10):105304

Talluru MK (2013) Manipulating large-scale structures in a turbulent boundary layer using a wall-normal jet. Ph.D. thesis, University of Melbourne

Townsend AA (1976) The structure of turbulent shear flow. Cambridge University Press, Cambridge

Tropea C, Yarin AL, Foss JF (2007) Springer handbook of experimental fluid mechanics, vol 1. Springer, Berlin

Van Dijk A, Nieuwstadt FTM (2004) The calibration of (multi-) hot-wire probes. 2. Velocity-calibration. Exp Fluids 36(4):550–564

Vincenti P, Klewicki JC, Morrill-Winter C, White CM, Wosnik M (2013) Streamwise velocity statistics in turbulent boundary layers that spatially develop to high Reynolds number. Exp Fluids 54(12):1–13

Vukoslavcevic P, Wallace JM, Balint J-L (1991) The velocity and vorticity vector fields of a turbulent boundary layer. Part 1.

simultaneous measurement by hot-wire anemometry. J Fluid Mech 228:25–51

Wallace JM, Foss JF (1995) The measurement of vorticity in turbulent flows. Ann Rev Fluid Mech 27(1):469–514

Wei T, Fife P, Klewicki J, McMurtry P (2005) Properties of the mean momentum balance in turbulent boundary layer, pipe and channel flows. J Fluid Mech 522:303–327

Willmarth WW, Bogar TJ (1977) Survey and new measurements of turbulent structure near the wall

Woodcock JD, Marusic I (2015) The statistical behaviour of attached eddies. Phys Fluids (1994-present) 27(1):015104